Dynamics of rising bubble population undergoing mass transfer and coalescence in highly viscous liquid

Franck Pigeonneau, L. Pereira, A. Laplace

Dynamics of rising bubble population undergoing mass transfer and coalescence in highly viscous liquid

F. Pigeonneau[a], L. Pereira[b], A. Laplace[c]

[a] *MINES Paris, PSL Research University, CEMEF - Centre for material forming, CNRS UMR 7635, CS 10207, rue Claude Daunesse 06904 Sophia Antipolis Cedex, France*
[b] *Ludwig-Maximilians-Universität München, Department of Earth and Environmental Sciences, Theresienstraße 41, 80333 Munich, Germany*
[c] *CEA, DES, ISEC, DE2D, University of Montpellier, Marcoule, France*

Abstract

The two-phase flow dynamics involving mass transfer and coalescence is investigated. The model is specifically developed to describe the dynamics of bubble population dispersed in glass forming liquids. The amounts of gas dissolved in the liquid are determined using the chemical equilibrium involving oxidation-reduction reactions. The gravitational bubble rising is used to write the coalescence kernel for which a collision efficiency is also introduced.

Based on a Direct Quadrature Method of Moments (DQMOM), a numerical method is developed. This numerical tool is applied to melting of borosilicate glass beads for which temperature and residence time of the sample in a crucible are investigated. The bubble density decreases sharply at short times. This early stage decrease is well explained and quantified when the coalescence is taken into account in numerical computations. The bubble size density is very well described with a log-normal distribution. Using the first three moments, the bubble size distribution obtained numerically is in good agreement with experimental data.

Numerical computations are also applied to soda-lime-silica glass in which the bubble release is driven by the mass transfer between the two phases. The faster decrease of bubble density than would be expected by temperature is reproduced by the numerical computation. The enhancement of the bubble release rate is mainly due to the increase of dissolved gas species with temperature.

Keywords: Population balance equation; glass forming liquid; coalescence; mass transfer; method of moments

*Corresponding author: Tel. +33 (4) 93 95 74 34.
Email address: franck.pigeonneau@minesparis.psl.eu (F. Pigeonneau)

1. Introduction

Multiphase and in particular bubbly flows are present in geophysics with the outgassing of volcanoes [1], in agribusiness industry with sparkling wines [2], in metallurgy in which bubbles are used to stir molten metal or enhance the heat and mass transfer [3], in power plants with boiling water in nuclear reactors [4], among others. Here, investigations are focused in glass melting process in which outgassing process is a major phenomena leading to strong limitations in industrial plants. Understanding how bubbles appear, disappear, interact, grow remains fundamental and applied issues.

In glass melting process, the bubble generation occurs mainly during the melting of raw materials. As generally accepted, bubbles are created due to the trapping of atmospheric gases and the decomposition of mineral species used as batch components [5]. As already shown long time ago by one of a first contribution devoted to fining process (impurity release) [6], the bubble release is mainly driven by the temperature. Recent experiments of glass cullet melting in a small crucible confirm this assertion [7, 8]. Pereira et al. [8] pinpointed that the bubble dynamics (bubble density, mean radius) can be rescaled by the residence time of a bubble in the bath directly linked to the temperature via the dynamical viscosity. Cable [9] underlined that bubble coalescence can play a role in the dynamics in the early stages of the process. In the review paper, Cable [10] pointed out the "*rate of refining,* [i.e. rate of bubble release,] *varies more with temperature than would be expected from the effects of temperature on bubble size and viscosity*". Predict the dynamics of bubble population undergoing gravitational rising, mass transfer and coalescence is a task not completely fulfilled. Consequently, the main purpose of this article is to study bubble populations rising in glass forming liquid undergoing mass transfer and coalescence.

Describe the dynamics of a population undergoing processes such as mass transfer and coalescence needs a model based on the population balance equation developed long time ago by Randolph and Larson [11] and Hulburt and Katz [12]. Today, this theory becomes primordial to study dispersed media. This theory has been presented by Ramkrishna [13] for a large range of applications. Despite these contributions, the theory was mainly limited to spatial homogeneous problems. A new step was overcame with the major contribution of Marchisio and Fox [14] in which the theory and numerical methods are applied to spatial inhomogeneous cases allowing the introduction of such theory in Computational Fluid Dynamics software.

In the context of glass science, the population balance theory has been initially proposed by Ungan et al. [15] to study the bubble density and the momentum coupling with the carrier phase. Nevertheless, the chemical process is completely ignored. Ungan et al. [16] investigated the silica grain dissolution in a glass bath with the same approach.

Roi et al. [17] developed a model to describe the bubble removal using a population balance equation with only mass transfer process. Balkanli and Ungan [18] improved the previous model by introducing a description of the bubble size distribution and the mass transfer with only one species (CO_2). Bensberg and Breitbach [19] described the bubble population assuming a predefined bubble size distribution corresponding to a log-normal distribution and further solved the equations of first three moments to characterize the bubble size distribution. Only one gas species is considered and the coupling is limited to the momentum balance. Pilon et al. [20] proposed a population balance equation in which the general aspect of the glass chemistry is described. The chemical reaction of fining agents is seen as an irreversible chemical reaction. Pilon and Viskanta [21] applied the previous model on the modeling of a glass furnace limiting to two gas species using a modified characteristic method to solve the population balance equation [22] without coalescence. Finally, Oda and Kaminoyama [23] studied the fining process coupling with the bubble density conservation in two dimensional geometry.

Despite these contributions, the development of the population balance equation taking into account mass transfer and coalescence in glass melting process is not yet provided. This is the main purpose of this contribution which is an extended version of the theoretical model developed in [24]. First, problem statement is detailed in section 2 in which mass transfer and coalescence processes are presented. The direct quadrature method of moments (DQMOM) is described in section 3. Numerical computations detailed in section 4 are based on experimental observations done in [8, 6]. Few conclusions are finally drawn in section 5. Appendix A provides numerical data needed to achieve the numerical computations.

2. Problem statement

2.1. Bubble state in phase space

The overall dynamics of a bubble population dispersed in a glass forming liquid involves mass transfer between the dispersed and continuous phases, coalescence among others. According to Ramos [25], and Pigeonneau [26], a bubble is composed by various gas species coming from the atmosphere above the glass bath, and from the liquid itself. Typically, gas species such as CO_2, N_2, H_2O, O_2 and SO_2 are involved. According to Hulburt and Katz [12], the dynamics of a dispersed phase depends on external coordinates corresponding to the spacial position where inclusions are localized and internal coordinates characterizing the state of each particle. In the following, the temperature is assumed uniform and constant in time.

Using the general drag force acting on a bubble [27, 28], the time scale required to reach the steady-state regime is proportional to a^2/ν with a the bubble radius and ν

the kinematic viscosity of the liquid. The typical radius is around tens of micrometres and the kinematic viscosity is around $10^{-2}\,\mathrm{m}^2/\mathrm{s}$ [8]. Consequently, a^2/ν is order of magnitude of $10^{-9}\,\mathrm{s}$ sufficiently small to neglect the bubble inertia. The bubble velocity is then removed from the internal coordinates since it can be explicitly determined. The relative bubble velocity is given by the terminal rising velocity according to Hadamard [29] and Rybczynski [30].

In principle, the rate of variation of the bubble radius requires the writing of the Rayleigh-Plesset equation [31] given by

$$\rho\left[a\ddot{a}+\frac{3}{2}\dot{a}^2\right]=P-P_0-\frac{2\gamma}{a}-\frac{4\eta}{a}\dot{a}, \tag{1}$$

with ρ the density of the liquid, P the pressure inside the bubble and P_0 the pressure in the liquid without the hydrostatic contribution, γ the surface tension and η the dynamic viscosity.

The normalization of the Rayleigh-Plesset equation with the atmospheric pressure leads to the inertia time scale of bubble variation equal to $a\sqrt{\rho/P_0}$. Moreover, the time scale of the viscosity term is given by η/P_0. These two characteristic times are around 10^{-6} to $10^{-5}\,\mathrm{s}$. Since the time scale due to the bubble rising over a distance equal to the bubble radius, $\nu/(ga)$, is larger than $10\,\mathrm{s}$ and the time scale of the mass transfer is in general much larger than the rising time, a quasi-static state can be used to determine the bubble pressure.

As already done by Pilon et al. [20], the molar fractions are considered as internal coordinates to take into account the multi-component bubble composition. External coordinates are $\boldsymbol{r}$, i.e. the position in space. Internal variables are bubble radius a and the molar fractions $\mathrm{x}_{g,i}$ with $i=1$ to N_g-1 and N_g the number of the gas species. Recall that the sum of the molar fractions over index i is equal to one. According to Pigeonneau [26], the rate of variation of $\boldsymbol{r}$, a and $\mathrm{x}_{g,i}$ are

$$\boldsymbol{v} = \boldsymbol{u}-\frac{\boldsymbol{g}a^2}{3\nu}, \tag{2}$$

$$\dot{a} = \frac{1}{2a}\sum_{i=1}^{N_g}\mathrm{Sh}(\mathrm{Pe}_i)\mathcal{H}_i\mathcal{D}_i\left(\mathrm{x}_{l,i}-\mathrm{x}_{g,i}\right), \tag{3}$$

$$\dot{\mathrm{x}}_{g,i} = \frac{3}{2a^2}\sum_{j=1}^{N_g}\mathrm{Sh}(\mathrm{Pe}_j)\mathcal{H}_j\mathcal{D}_j\left(\delta_{ij}-\mathrm{x}_{g,i}\right)\left(\mathrm{x}_{l,j}-\mathrm{x}_{g,j}\right),\ \forall\ i=[1;N_g-1]. \tag{4}$$

In this system of equations, t is the time, $\boldsymbol{u}$ the velocity field of the continuous phase, $\boldsymbol{g}$ the gravity field, ν is the kinematic viscosity. In the growth rate of a, eq. (3), Sh is

the Sherwood number depending on the Péclet number given by

$$\mathrm{Pe}_i = \frac{2ga^3}{3\nu\mathcal{D}_i}. \tag{5}$$

In the creeping flow, the Sherwood number is strongly linked to the mobility of the bubble/liquid interface [32, 33]. While for immobile interface, the Sherwood number scales as $\sqrt[3]{\mathrm{Pe}}$, Sh is proportional to $\sqrt{\mathrm{Pe}}$ for mobile interface in the limit of high Péclet number. According to Pigeonneau et al. [34], the study on the shrinkage of O_2 bubble in glass forming liquid shows that the bubble/liquid interface can be considered as mobile. Consequently, the Sherwood number is determined by the correlation proposed by Clift et al. [33] equal to

$$\mathrm{Sh}(\mathrm{Pe}) = 1 + \left(1 + 0.564\,\mathrm{Pe}^{2/3}\right)^{3/4}. \tag{6}$$

The quantity $\mathcal{H}_i$ is the dimensionless solubility given as a function of the Henry coefficient

$$\mathcal{L}_i = \frac{C_i^s}{P_i} \tag{7}$$

by [35]

$$\mathcal{H}_i = RT\mathcal{L}_i, \tag{8}$$

with R the perfect gas constant and T the temperature in K. In eq. (7), C_i^s is the molar concentration at the interface between the liquid and the atmosphere in which the gas species has a partial pressure equal to P_i. In eqs. (3) and (4), $\mathcal{D}_i$ is the diffusion coefficient of the species i in the liquid. The dimensionless variable $\mathrm{x}_{l,i}$ corresponds to the gas saturation in the liquid of the i species defined by

$$\mathrm{x}_{l,i} = \frac{C_i^l}{\mathcal{L}_i P}, \tag{9}$$

in which C_i^l is the molar concentration of the gas species dissolved in the liquid. According to Pigeonneau [26], the effects of the hydrostatic and Laplace pressures can be neglected. The total pressure in each bubble P is assumed equal to the atmospheric pressure above the liquid bath.

2.2. Population balance equation

Integration of equations (2-4) associated with initial conditions gives a particular trajectory in the phase space $(\boldsymbol{r}, a, \mathbf{x}_g)$ with $\mathbf{x}_g = (\mathrm{x}_{g,1}, \cdots, \mathrm{x}_{g,N_g-1})$. Applied to a large number of bubbles, a density function can be defined in the limit of the large number of particles written $f(\boldsymbol{r}, t; a, \mathbf{x}_g)$ in which by convention the Eulerian variables $(\boldsymbol{r}, t)$ has been separated by a semicolon of the internal coordinates. This function is assumed

sufficiently smooth to be differentiable [14]. From this definition $f(\boldsymbol{r}, t; a, \mathbf{x}_g)d\boldsymbol{r}dad\mathbf{x}_g$ is the number of inclusions in an elementary hyper-volume embodied between $\boldsymbol{r}$ and $\boldsymbol{r}+d\boldsymbol{r}$, a and $a+da$, $\mathbf{x}_g$ and $\mathbf{x}_g + d\mathbf{x}_g$. According to Ramkrishna [13] and Marchisio and Fox [14], the balance equation of population is given by

$$\frac{\partial f}{\partial t} + \boldsymbol{\nabla} \cdot (\boldsymbol{v} f) + \frac{\partial (\dot{a} f)}{\partial a} + \sum_{i=1}^{N_g - 1} \frac{\partial (\dot{\mathrm{x}}_{g,i} f)}{\partial \mathrm{x}_{g,i}} = h(\boldsymbol{r}, t; a, \mathbf{x}_g), \tag{10}$$

in which $\boldsymbol{v}$, $\dot{a}$ and $\dot{\mathrm{x}}_{g,i}$ are the right-hand side of eqs. (2-4) respectively and h is a source term resulting of the birth and the death of bubbles due to coalescence, breakup or nucleation.

The mass transfer between the bubble population changes the amount of dissolved gas in the liquid which can be introduced in molar conservation of the gas species i as follows

$$\frac{\partial \mathrm{x}_{l,i}}{\partial t} + \boldsymbol{\nabla} \cdot (\boldsymbol{u} \mathrm{x}_{l,i}) = \mathcal{D}_i \boldsymbol{\nabla}^2 \mathrm{x}_{l,i} - 2\pi \int_0^\infty \int_{\Omega_{\mathbf{x}_g}} a \, \mathrm{Sh}(\mathrm{Pe}_i) \mathcal{D}_i (\mathrm{x}_{l,i} - \mathrm{x}_{g,i}) f(\boldsymbol{r}, t; a, \mathbf{x}_g) d\mathbf{x}_g da, \tag{11}$$

for all $i \in [1, N_g]$. The domain $\Omega_{\mathbf{x}_g}$ in the space $\mathbf{x}_g$ is equal to $[0, 1]^{N_g - 1}$.

To solve the population balance equation, a size-conditioned density is defined as follows [36, 14]

$$n(\boldsymbol{r}, t; a) = \int_{\Omega_{\mathbf{x}_g}} f(\boldsymbol{r}, t; a, \mathbf{x}_g) d\mathbf{x}_g, \tag{12}$$

and a size-conditioned of a quantity G is then defined by

$$\langle G | a \rangle = \frac{\displaystyle\int_{\Omega_{\mathbf{x}_g}} G f(\boldsymbol{r}, t; a, \mathbf{x}_g) d\mathbf{x}_g}{n(\boldsymbol{r}, t; a)}. \tag{13}$$

The moment of the k order is given by

$$\mu_k(\boldsymbol{r}, t) = \int_0^\infty a^k n(\boldsymbol{r}, t; a) da. \tag{14}$$

The zeroth order moment is simply the bubble density. The second order moment is proportional to the interfacial area concentration and the third order moment is proportional to the volume fraction of bubble.

The population balance equation applied to $n(\boldsymbol{r}, t; a)$ is then given by

$$\frac{\partial n}{\partial t} + \boldsymbol{\nabla} \cdot (\langle \boldsymbol{v} | a \rangle n) + \frac{\partial (\langle \dot{a} | a \rangle n)}{\partial a} = S(\boldsymbol{r}, t; a), \tag{15}$$

after integration over the total space of molar fractions with $S(\boldsymbol{r},t;a)$ the integral of $h(\boldsymbol{r},t;a,\mathbf{x}_g)$. Equation on the gas saturation becomes

$$\frac{\partial \mathrm{x}_{l,i}}{\partial t}+\boldsymbol{\nabla}\cdot(\boldsymbol{u}\mathrm{x}_{l,i})=\mathcal{D}_i\boldsymbol{\nabla}^2\mathrm{x}_{l,i}-2\pi\int_0^\infty a\,\mathrm{Sh}(\mathrm{Pe}_i)\mathcal{D}_i(\mathrm{x}_{l,i}-\langle \mathrm{x}_{g,i}|a\rangle)n(\boldsymbol{r},t;a)da. \quad (16)$$

2.3. Coalescence source term

The release of bubbles in a molten glass is mainly driven by the buoyancy force. Due to large initial bubble density, collision and coalescence are strongly likely to happen. The source term $S(\boldsymbol{r},t;a)$ due to the coalescence process is equal to [14]

$$S(\boldsymbol{r},t;a)=\frac{1}{2}\int_0^a\frac{a^2}{\left(a^3-a'^3\right)^{2/3}}K\left(a',\sqrt[3]{a^3-a'^3}\right)n(\boldsymbol{r},t;a')n\left(\boldsymbol{r},t;\sqrt[3]{a^3-a'^3}\right)da'-$$
$$n(\boldsymbol{r},t;a)\int_0^\infty K\left(a,a'\right)n(\boldsymbol{r},t;a')da', \quad (17)$$

with $K\left(a,a'\right)$ the coalescence kernel.

This quantity depends on the nature of the bubble motion and the kind of the flow, laminar or turbulent [37]. In the case of the bubble rising motion in creeping regime, $K\left(a,a'\right)$ is written as follows [38]

$$K\left(a,a'\right)=\frac{g\pi}{3\nu}\left(a+a'\right)^2\left|a^2-a'^2\right|E_{\mathrm{col}}\left(a,a'\right), \quad (18)$$

with $E_{\mathrm{col}}\left(a,a'\right)$ the collision efficiency. The physical meaning of this quantity is simply the ratio of the collision section due to hydrodynamic interactions divided by the collision section without interaction equal to $\pi\left(a+a'\right)^2$ [39, 38]. According to these two previous contributions, the coalescence efficiency in the limit of spherical bubbles taking into account the hydrodynamic interaction does not change significantly with the bubble ratio a/a' and is roughly equal to 0.2.

3. Direct quadrature method of moments

Various numerical methods have been developed over the years to solve the population balance equation. A first class of methods is based on a discretization of the internal coordinate. This kind of method has been used to study the rain formation by Kovetz and Olund [40]. A same approach has been used to study droplet population in homogeneous isotropic turbulence [41]. Finite element and orthogonal collocation have been developed by Gelbard and Seinfeld [42]. Ramkrishna [43] developed a method of weighted residuals with Laguerre function as trial functions (see also [44]). In the context of glass melting process, Pilon and Viskanta [22] determined directly the density function

using a reverse characteristic method. Hulburt and Katz [12] proposed to solve equations on the moments of the density function. To close the system of equations the density function is written with Γ-distribution and associated Laguerre polynomials [45].

Here, the direct quadrature method of moments initially proposed by Marchisio and Fox [46] is used. This method enables to take into account the various processes such as bubble growth, coalescence, break-up and nucleation phenomena with a simple closure procedure.

3.1. Spatial inhomogeneous formulation

In method of moments, the density function $n(\boldsymbol{r}, t; a)$ is written as a summation of Dirac delta functions as follows [46]

$$n(\boldsymbol{r}, t; a) = \sum_{\alpha=1}^{N} \omega_\alpha(\boldsymbol{r}, t)\delta\left[a - a_\alpha(\boldsymbol{r}, t)\right], \tag{19}$$

in which $\omega_\alpha(\boldsymbol{r}, t)$ is the weight of integration of the node (abscissa) $a_\alpha(\boldsymbol{r}, t)$ and N corresponds to the number of classes representing the density function. The $2N$ first moment equations are required to determine the N couples $(\omega_\alpha, a_\alpha)$. Generally, a product-difference [47] or Wheeler algorithms [48] are used to find the weights and abscissas. It is well-known that this kind of method can be ill-posed if two abscissas become equal.

To circumvent this difficulty, Marchisio et al. [49] proposed an alternative method to determine directly the N couples $(\omega_\alpha, a_\alpha)$. Before to detail the direct quadrature method of moments, a dimensionless form of (15) and (16) is written. Our main goal is to study the release of bubble population from a glass forming liquid in a crucible with a height H. According to Pereira et al. [8], the characteristic time is equal to $H\nu/(ga_0^2)$. The characteristic bubble radius a_0 is defined as follows

$$a_0 = \sqrt[3]{\frac{\mu_3}{\mu_0}}. \tag{20}$$

If N_0 is the initial bubble density in m^{-3}, the bubble density function $n\left(\boldsymbol{r}, t; a\right)$ is reduced by the ratio N_0/a_0. The velocity field is normalized by ga_0^2/ν and spatial coordinates by H, the liquid height. For convenient reason, dimensionless variables are written with the same symbols used previously meaning that the population balance equation (15) does not change. Bubble growth rate and the coalescence kernel are modified as

follows

$$\langle \dot{a}|a\rangle = \frac{1}{2a}\sum_{i=1}^{N_g} \mathrm{Sh}\left(\mathrm{Pe}_i\right)\mathcal{H}_i\,\mathrm{Fo}_i\left(\mathrm{x}_{l,i}-\langle \mathrm{x}_{g,i}|a\rangle\right), \tag{21}$$

$$K\left(a,a'\right) = \frac{K_0 E_{\mathrm{coa}}}{12}\left(a+a'\right)^2\left|a^2-a'^2\right|, \tag{22}$$

in which Fo_i corresponding to a Fourier number and K_0 are given by

$$\mathrm{Fo}_i = \frac{\nu H \mathcal{D}_i}{g a_0^4}, \tag{23}$$

$$K_0 = 4\pi N_0 a_0^2 H. \tag{24}$$

The rate of the size-conditioned molar fraction has to be written as follows

$$\langle \dot{\mathrm{x}}_{g,i}|a\rangle = \frac{3}{2a^2}\sum_{j=1}^{N_g}\mathrm{Sh}(\mathrm{Pe}_j)\mathcal{H}_j\,\mathrm{Fo}_j\left(\delta_{ij}-\langle \mathrm{x}_{g,i}|a\rangle\right)\left(\mathrm{x}_{l,j}-\langle \mathrm{x}_{g,j}|a\rangle\right),\ \forall\, i=[1;N_g-1]. \tag{25}$$

Finally, the transport equation in the saturation of the gas species i takes the following form

$$\frac{\partial \mathrm{x}_{l,i}}{\partial t}+\boldsymbol{\nabla}\cdot(\boldsymbol{u}\mathrm{x}_{l,i}) = \frac{a_0^2\,\mathrm{Fo}_i}{H^2}\boldsymbol{\nabla}^2\mathrm{x}_{l,i}-\frac{3\varphi_0}{2}\int_0^\infty a\,\mathrm{Sh}(\mathrm{Pe}_i)\,\mathrm{Fo}_i(\mathrm{x}_{l,i}-\langle \mathrm{x}_{g,i}|a\rangle)n(\boldsymbol{r},t;a)da, \tag{26}$$

with

$$\varphi_0 = \frac{4\pi a_0^3 N_0}{3}, \tag{27}$$

corresponding to the initial volume fraction of the bubble population. The coefficient K_0 given by eq. (24) characterizes also the initial bubble population. It is equal to the product of the interfacial area concentration by the crucible height. Physically, this dimensionless group can be seen as the surface area ratio of the bubble population to the free surface of the fluid domain. A large value of K_0 means that the coalescence is important and the mass transfer is mainly between the bubble population and the liquid.

According to Marchisio and Fox [49], the transport equations of the N couples $(\omega_\alpha, a_\alpha)$ are obtained by introduction of (19) in the population balance equation (15) which gives

$$\frac{\partial \omega_\alpha}{\partial t}+\boldsymbol{\nabla}\cdot(\boldsymbol{v}_\alpha\omega_\alpha) = A_\alpha, \tag{28}$$

$$\frac{\partial \zeta_\alpha}{\partial t}+\boldsymbol{\nabla}\cdot(\boldsymbol{v}_\alpha\zeta_\alpha) = B_\alpha, \tag{29}$$

with $\zeta_\alpha = \omega_\alpha a_\alpha$ and $\boldsymbol{v}_\alpha = \langle \boldsymbol{v}|a_\alpha\rangle$. The $2N$ right-hand sides A_α and B_α are solution of

the linear system

$$(1-k)\sum_{\alpha=1}^{N} a_\alpha^k A_\alpha + k\sum_{\alpha=1}^{N} a_\alpha^{k-1} B_\alpha = C_k,\ \forall\ k \in [0;2N], \tag{30}$$

and C_k is equal to

$$C_k = \sum_{\alpha=1}^{N}\sum_{\beta=1}^{N} \omega_\alpha\omega_\beta K(a_\alpha,a_\beta)\left[\frac{\left(a_\alpha^3+a_\beta^3\right)^{k/3}}{2} - a_\beta^k\right] + k\sum_{\alpha=1}^{N} a_\alpha^{k-1}\dot{a}_\alpha\omega_\alpha, \tag{31}$$

with $\dot{a}_\alpha = \langle \dot{a}|a_\alpha\rangle$ given by eq. (21) with the bubble size equal to a_α.

To close the growth rate, the $N_g - 1$ molar fractions and for each bubble class α written as $\langle \mathrm{x}_{g,i}|a_\alpha\rangle$ have to be solved using the following transport equation

$$\frac{\partial\langle \mathrm{x}_{g,i}|a_\alpha\rangle}{\partial t} + \boldsymbol{\nabla}\cdot(\boldsymbol{v}_\alpha\langle \mathrm{x}_{g,i}|a_\alpha\rangle) = \frac{3}{2a_\alpha^2}\sum_{j=1}^{N_g}\mathrm{Sh}(\mathrm{Pe}_{j,\alpha})\mathcal{H}_j\,\mathrm{Fo}_j\left(\delta_{ij} - \langle \mathrm{x}_{g,i}|a_\alpha\rangle\right)\left(\mathrm{x}_{l,j} - \langle \mathrm{x}_{g,j}|a_\alpha\rangle\right), \tag{32}$$

$\forall\ i = [1; N_g - 1]$. Quantity $\mathrm{Pe}_{j,\alpha}$ is the Péclet number given by (5) based on the bubble size a_α. Finally the N_g gas saturations are solution of

$$\frac{\partial \mathrm{x}_{l,i}}{\partial t} + \boldsymbol{\nabla}\cdot(\boldsymbol{u}\mathrm{x}_{l,i}) = \frac{a_0^2\,\mathrm{Fo}_i}{H^2}\boldsymbol{\nabla}^2\mathrm{x}_{l,i} - \frac{3\varphi_0}{2}\sum_{\alpha=1}^{N} a_\alpha\omega_\alpha\,\mathrm{Sh}(\mathrm{Pe}_{i,\alpha})\,\mathrm{Fo}_i(\mathrm{x}_{l,i} - \langle \mathrm{x}_{g,i}|a_\alpha\rangle). \tag{33}$$

The total number of equations to solve the dispersed phase is equal to $2N + N(N_g - 1)$ completed by the N_g transport equations on $\mathrm{x}_{l,i}$. The system of equations is close to the previous one provided by Pigeonneau [24] to study the interaction between a bubble population and the chemistry of glass forming liquid without the interaction between bubble classes.

3.2. Spatial homogeneous formulation

The previous system of equations needs to be completed by the balance equations to determine the velocity and the pressure of the continuous phase. Since our main objective is to compare with experiments achieved in a crucible in which only volume averages data are known, only spatial homogeneous formulation is presented and solved in the following. To determine the volume average equations, the appropriate method is to first average the population balance equation which becomes

$$\frac{\partial\langle n\rangle}{\partial t} + \frac{\partial(\langle \dot{a}|a\rangle\langle n\rangle)}{\partial a} = \langle S\rangle(t;a) - \frac{\langle n\rangle a^2}{3}, \tag{34}$$

in which $\langle\rangle$ corresponds to the volume average. The extra sink term of the right-hand side of the previous equation represents the bubble release through the free surface of the glass bath. In this formulation, the mass interaction between the liquid and the atmosphere is neglected at the free surface of the domain. This assumption is justified when the K_0 product is larger than one. This will be fulfilled in the next section.

The development of the direct quadrature method of moments does not change. In this case, all quantities are averaged on the total volume of the domain. The ordinary differential equations are then the following

$$\frac{d\omega_\alpha}{dt} = A_\alpha, \forall\alpha \in [1, N], \tag{35}$$

$$\frac{d\zeta_\alpha}{dt} = B_\alpha, \forall\alpha \in [1, N], \tag{36}$$

$$\frac{d\langle \mathrm{x}_{g,i}|a_\alpha\rangle}{dt} = \frac{3}{2a_\alpha^2}\sum_{j=1}^{N_g}\mathrm{Sh}(\mathrm{Pe}_{j,\alpha})\mathcal{H}_j\,\mathrm{Fo}_j\left(\delta_{ij} - \langle \mathrm{x}_{g,i}|a_\alpha\rangle\right)\left(\mathrm{x}_{l,j} - \langle \mathrm{x}_{g,j}|a_\alpha\rangle\right), \quad \forall i \in [1, N_g - 1], \tag{37}$$

$$\frac{d\mathrm{x}_{l,i}}{dt} = -\frac{3\varphi_0}{2}\sum_{\alpha=1}^{N} a_\alpha\omega_\alpha\,\mathrm{Sh}(\mathrm{Pe}_{i,\alpha})\,\mathrm{Fo}_i(\mathrm{x}_{l,i} - \langle \mathrm{x}_{g,i}|a_\alpha\rangle), \ \forall i \in [1, N_g]. \tag{38}$$

The N couples (A_α, B_α) are always solution of (30) but C_k takes the following form

$$C_k = \sum_{\alpha=1}^{N}\sum_{\beta=1}^{N}\omega_\alpha\omega_\beta K(a_\alpha, a_\beta)\left[\frac{\left(a_\alpha^3 + a_\beta^3\right)^{k/3}}{2} - a_\beta^k\right] + k\sum_{\alpha=1}^{N} a_\alpha^{k-1}\langle\dot{a}|a_\alpha\rangle\omega_\alpha - \sum_{\alpha=1}^{N}\frac{\omega_\alpha a_\alpha^{k+2}}{3}, \tag{39}$$

with $\langle\dot{a}|a_\alpha\rangle$ given by eq. (21) with the bubble size equal to a_α.

Initially, the bubble size distribution is imposed using results obtained in [8]. Using a Wheeler algorithm, weight and abscissa of the α class are determined at t equal zero. The system of ordinary differential equations, (35-38) completed by (39) and (21) is solved using a Runge-Kutta method at the fourth order. The software is accessible in the github platform, see the link given at the end of the article.

4. Results and discussion

4.1. Glass melting of borosilicate glass beads

To study experimentally the dynamics of the bubble in a glass forming liquid, glass powders are prepared from synthesized borosilicate glasses. The accurate composition

can be found in [8]. Sizes of the granular media are in the range of (250-500) µm. The glass powder is introduced in a cylindrical alumina crucible with an inner diameter equal to 28 mm and a height equal to 40 mm. The density of the glass forming liquid is taken equal to 2270 kg/m^3 [50]. The dynamic viscosity is a function of the temperature determined from the Vogel-Fulcher-Tammann's law [51] as follows

$$\eta(T) = 8.39 \cdot 10^{-3} \exp\left(\frac{6026.88}{T - 610.16}\right), \tag{40}$$

with T in Kelvin. The glass transition temperature is found equal to 523 °C and the softening (Littleton) temperature is equal to 637 °C. The former is defined for $\eta(T_g)$=10^{12} Pa s, while the latter for $\eta(T_s) = 10^{6.65}$ Pa s [52]. The Littleton temperature corresponds to the value above which the media collapses under its own weight.

After filling, each crucible is introduced in a furnace controlled in temperature during a certain time. When the desired residence time is over, the crucible is removed from the furnace to be cooled down until the room temperature. Each crucible is cut from the middle. One half is mounted in epoxy resin and then polished for optical microscope imaging. Figure 1 presents binarized optical microscope images obtained for T equal to 1000 and 1100 °C. Three melting times are shown at 20, 40, and 60 min. At 20 min and 1000 °C, the sample has a large population of small bubbles in comparison to the sample at the same melting time but at 1100 °C. For longer times at 1000 °C, samples show that the bubble population stays relatively elevated. Heterogeneity is clearly visible in Figure 1. Large bubbles are observed close to the crucible walls. The largest bubbles are mainly localized close to the vertical boundaries of the crucible and to the free surface. For T equal to 1100 °C, the bubble population decreases strongly with time. A large fraction of tiny bubbles in the two bottom corners is observed for T equal to 1100 °C and a residence time of 60 min. Remark that the free surface are strongly curved while it is not expected at a temperature larger than T_s [7]. This effect comes from the thermal cooling leading to a thermal contraction of the gas phase and also a shrinkage due to the glass transition temperature.

From the binarized optical microscope images, an analysis is done to determine the bubble numbers by surface unit, the surface fraction and average size over the time. A detailed presentation has been already published in [8]. Since the theoretical model has been developed for a 3D configuration, the 2D data obtained by image analysis from the cut views depicted in Figure 1 must be converted in 3D data. To do so, the general principle of the stereology [53] is used. Mainly, the equality between the surface fraction and volume fraction is used to determine the bubble volume density. Since the bubble dimensions are determined at room temperature, a correction is applied to estimate the

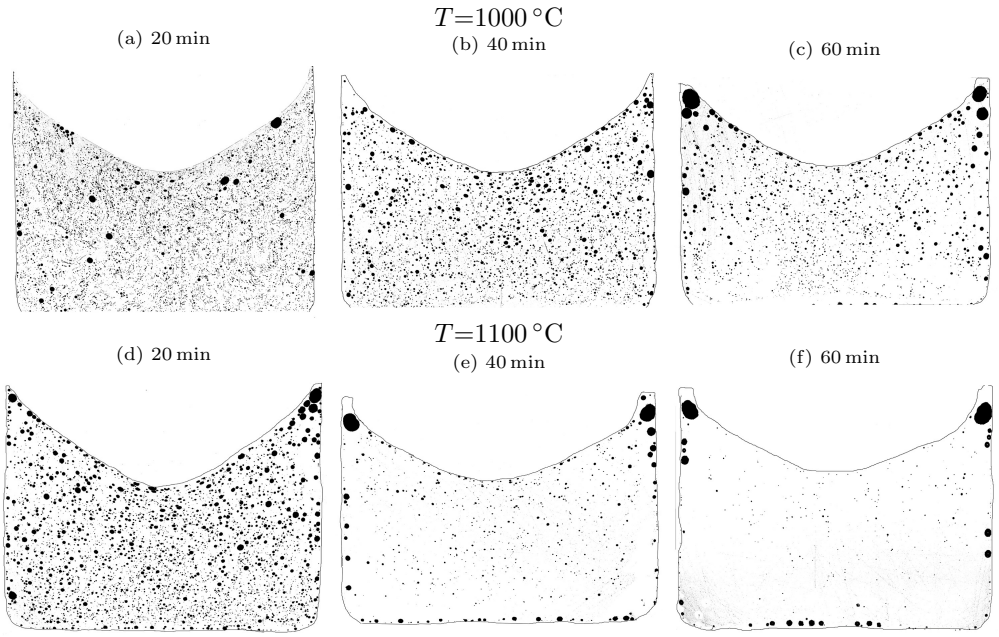

Figure 1: Binarized optical microscope images of samples for two temperatures and three melting times.

bubble size and volume at the temperature T. The glass forming liquid behaves like a solid when the temperature becomes smaller that the softening temperature, T_s. The volume correction is determined by multiplied the bubble volume at room temperature by a factor T/T_s. For the radius, the factor is $\sqrt[3]{T/T_s}$.

The initial conditions for the numerical computations are taken from the experimental data for the smallest residence time, i.e. 20 min. The relevant parameters for T equal to 1000, 1050 and 1100 °C are reported in Table 1. The initial bubble density is a huge quantity of bubbles since in a volume of one cubic millimeter, the number of bubbles reaches more than few hundreds. This relative large amount of bubbles is related to a small granulometry of the initial glass beads as seen by Boloré et al. [7]. It is important to stress that the volume fraction is small in comparison of the expected value in the original granular media. Due to the collapse of glass beads during the heating, large quantity of the gas phase are removed from the liquid [7]. Consequently, the height of the liquid is roughly reduced by a factor two. Even if the crucible is fully filled of granular media at room temperature, the height of liquid during the residence of the crucible in the furnace is taken equal to one-half of the crucible height, i.e. 20 mm. For the three temperatures, the values of K_0 are always larger than one meaning that the coalescence is expected to be the most relevant phenomena. As already pointed out above, the K_0 product is the area ratio of the bubble population to the free surface of the crucible. This

Table 1: Initial bubble density, φ_0 and K_0 used in the numerical computation for three temperatures.

T (°C)	N_0 (m^{-3})	φ_0	K_0
1000	3.45×10^{11}	1.21×10^{-1}	165.96
1050	1.90×10^{11}	1.47×10^{-1}	155.00
1100	6.88×10^{10}	1.68×10^{-1}	121.00

Table 2: Parameters μ and σ of the log-normal distribution, eq. (41) for the three temperatures.

T (°C)	μ	σ
1000	3.34	0.54
1050	3.57	0.56
1100	3.72	0.68

means that the surface exchange is roughly around one hundred more efficient through the bubble surface than from the free surface.

Bubble size distributions are determined from images taken at 20 min. The probability density functions under histogram form and for each temperature are depicted in Figure 2. Due to a limit of the bubble detection, there is no bubbles for radius smaller than 15 µm. The bubble size distribution is more and more spread when the temperature increases. As already found in [7], the bubble size distribution is well described by a log-normal distribution written as follows

$$f(a,\mu,\sigma) = \frac{1}{a\sigma\sqrt{2\pi}} \exp\left[-\frac{(\ln a - \mu)^2}{2\sigma^2}\right]. \tag{41}$$

The two dimensionless coefficients, μ and σ are computed from the mean radius and the variance of experimental data. The numerical values are reported in Table 2 for a size bubble distribution determined in µm^{-1}.

Solid lines in Figure 2 are the log-normal distributions using the data of Table 2. As underlined in [7], the bubble density function is well described by a log-normal distribution because the void in the initial granular material follows a log-normal distribution as shown by Reboul et al. [54].

In the following, numerical computations are achieved with N equal to 3. The log-normal distribution obtained at each temperature is used to determine the initial values of a_α and ω_α by the Wheeler algorithm for α equal from 1 to 3. Since each couple $(a_\alpha, \omega_\alpha)$ is a Dirac representation of the bubble distribution, Figure 2 provides also the two first couples $(a_\alpha, \omega_\alpha)$. The two first classes exhibit the largest magnitude centered in the range of radius where the probability density function is important. For both temperature, the weight of the last class is very small and the respective abscissa is out of the range of the x axis of Figure 2.

(a) T=1000 °C (b) T=1050 °C

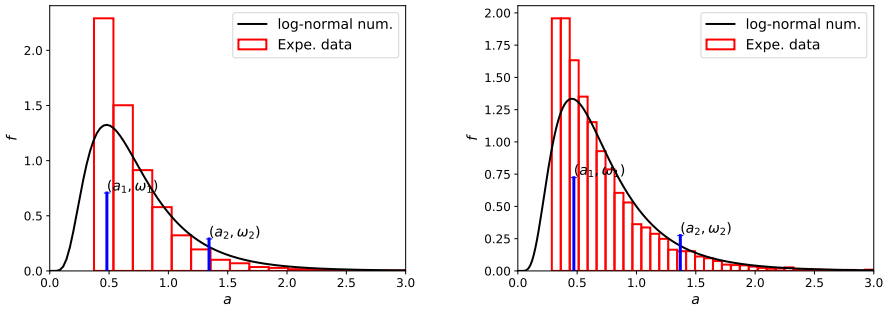

(c) T=1100 °C

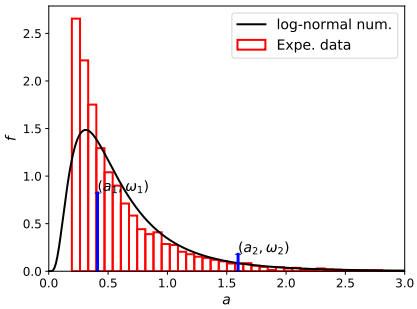

Figure 2: Initial normalized probability density function as a function of a determined from image analysis for the three temperatures at 20 min. Log-normal distribution and the amplitudes of initial ω_α are also reported for α equal 1 and 2.

From these data, numerical computations solving the problem presented in the previous section have been done for the three temperatures of the experiment. Three gas species are considered: O_2, N_2 and CO_2. Since the bubble formation is mainly due to the collapse of the liquid when the temperature becomes larger than the softening temperature, the initial composition of bubbles is taken close to the air composition. According to Pereira et al. [8], the molar fractions of O_2, N_2 and CO_2 are initially taken equal to 0.2, 0.7 and 0.1 respectively. Solubilities and diffusion coefficients are gathered in Appendix A. The concentrations of dissolved gas in the liquid has been determined using the oxidation-reduction reaction of cerium given by

$$\mathrm{Ce}^{4+} + \frac{1}{2}\mathrm{O}^{2-} \rightleftharpoons \mathrm{Ce}^{3+} + \frac{1}{4}\mathrm{O}_2. \tag{42}$$

The equilibrium constant of this reaction is given by

$$K_{\mathrm{Ce}} = \frac{C^l_{\mathrm{Ce^{3+}}} \sqrt[4]{C^l_{\mathrm{O_2}}}}{C^l_{\mathrm{Ce^{4+}}}} = \exp\left(-\frac{\Delta G_{\mathrm{Ce}}}{RT}\right), \tag{43}$$

with $C^l_{\mathrm{Ce^{4+}}}$, $C^l_{\mathrm{Ce^{3+}}}$ the molar concentration of Ce^{4+} and Ce^{3+} in the liquid. The Gibbs energy is written as follows

$$\Delta G_{\mathrm{Ce}} = \Delta H_{\mathrm{Ce}} - T\Delta S_{\mathrm{Ce}}. \tag{44}$$

The enthalpy and entropy of the reaction (42) has been determined by Pinet et al. [55] and are given in Appendix A. Nitrogen and carbon oxide have a molar concentrations equal to $10^{-2}\,\mathrm{mol/m^3}$ and $4\times10^{-2}\,\mathrm{mol/m^3}$ respectively. Data needed to compute solubilities and diffusion coefficients are given in Appendix A.

To measure the relevance of the coalescence phenomena, numerical simulations have been done with and without the coalescence source term. Figure 3 depicts the zeroth order moment corresponding to the bubble density as a function of the normalized time. This quantity is normalized by the initial bubble density. The solid line is the result obtained with coalescence and the dashed line without coalescence. Black dots are the experimental data.

While without coalescence source term, μ_0 decreases slowly due to the release of the bubble from the crucible, the behavior changes dramatically when the coalescence is accounted for. A fast decrease of the bubble density is observed at short experimental durations. This first stage is followed by a small decrease of bubble as a function of time. This general behavior is found regardless of temperature. Numerical computations achieved with coalescence reproduce very well the experimental observations. In the early stages, the coalescence is the main phenomena involved in the bubble dynamics rising in the glass forming liquid as proposed by Cable [9]. The coalescence efficiency has been taken equal to 0.175 to obtain the best comparison for the three temperatures.

With the decrease of the bubble density, coalescence events are scarcer and scarcer since the source term of the coalescence is proportional to the square of the probability density function. These numerical results justify also to consider a coalescence kernel due to the bubble rising. The coalescence becomes negligible when the zeroth moment decrease of one order of magnitude. The relevance of the coalescence is measured by the magnitude of K_0 given by eq. (24). As reported in Table 1, the value of K_0 computed with the bubble densities at the smallest residence time in the crucible is order to few tens. With a decrease of the bubble density of one order of magnitude, the importance of the coalescence becomes relevant when K_0 is larger than one. The bubble density should

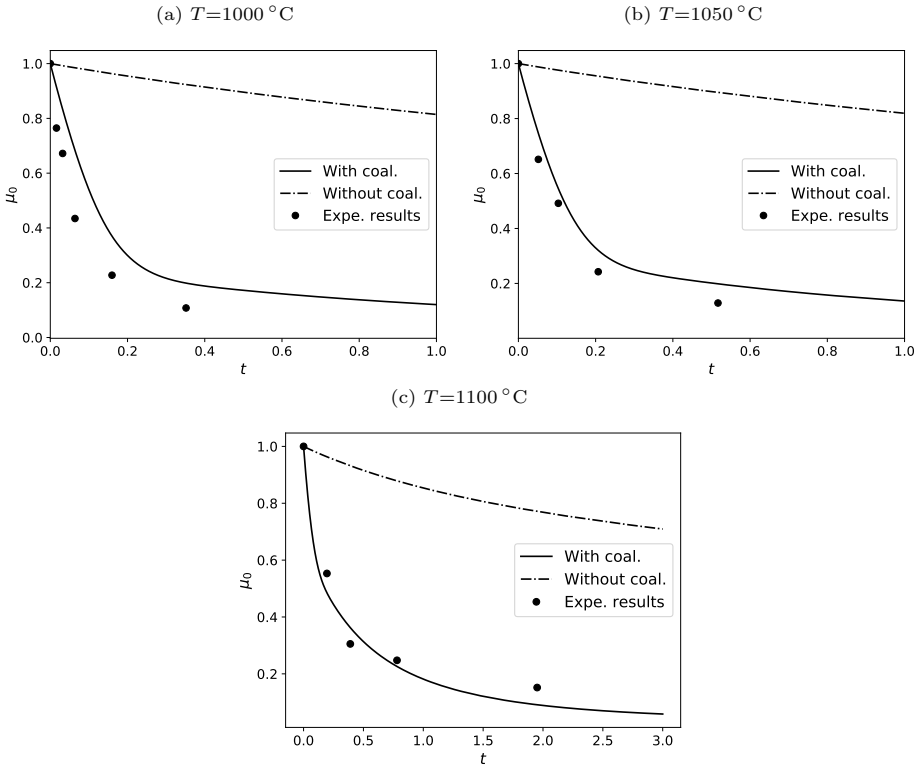

Figure 3: μ_0 as a function of t obtained numerically with and without coalescence and experimentally for three temperatures.

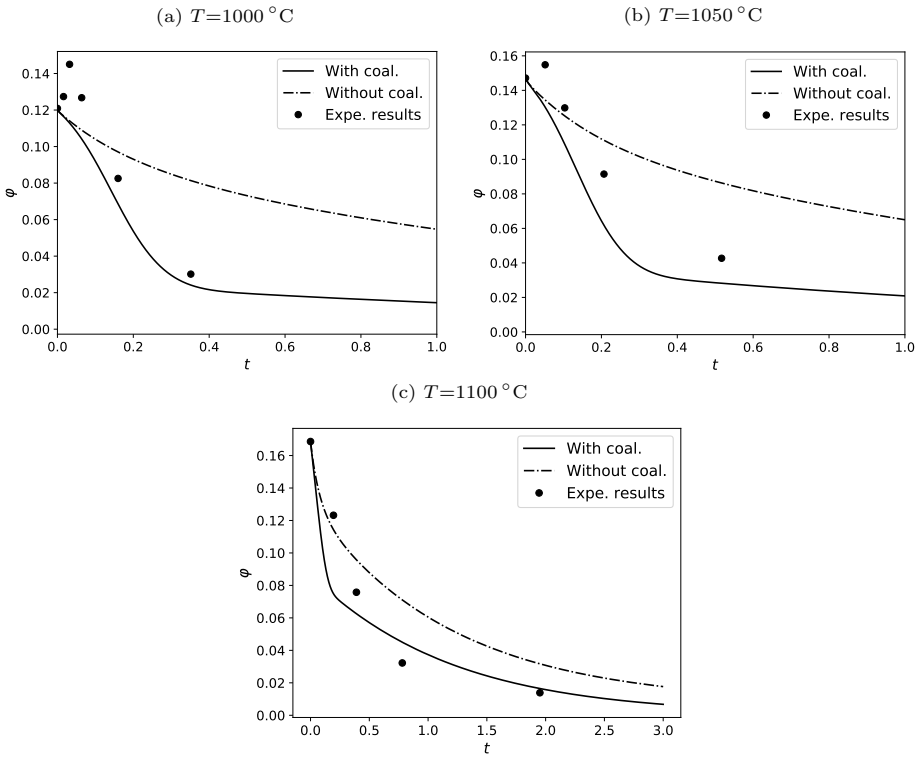

Figure 4: $\varphi = 4\pi\mu_3/3$ as a function of t obtained numerically with and without coalescence and experimentally for three temperatures.

be larger than $10^2\,\mathrm{cm}^{-3}$ to have a significant effect of the coalescence. In other words, the probability of coalescence is mainly linked to distance between two bubbles. Since the distance separating two bubbles is proportional to $1/\sqrt[3]{N_0}$ [56], the probability of coalescence becomes relevant when the distance between two bubbles is less than 1 mm.

Figure 4 presents the behavior of the volume fraction as a function of normalized time. Once again, the effect of the coalescence is clear. The comparison with experimental results is less satisfying. The unexpected increase of volume fraction at short times is due to an experimental artifact. Bubbles with a size smaller than the detection threshold are not taken into account in the volume fraction at short times. Due to the bubble dynamics, these tiny bubbles become enough large to be detected for larger residence times. This artifact disappears for T equal to 1100 °C. It is mainly due to the faster bubble dynamics leading to observation of tiny bubbles at the first residence times. Apart from this beginning, experiments exhibits a strong decrease of the volume fraction with a rate close to this one determined numerically.

The probability density functions after 2 h in the furnace are determined from ex-

(a) T=1000 °C (b) T=1050 °C

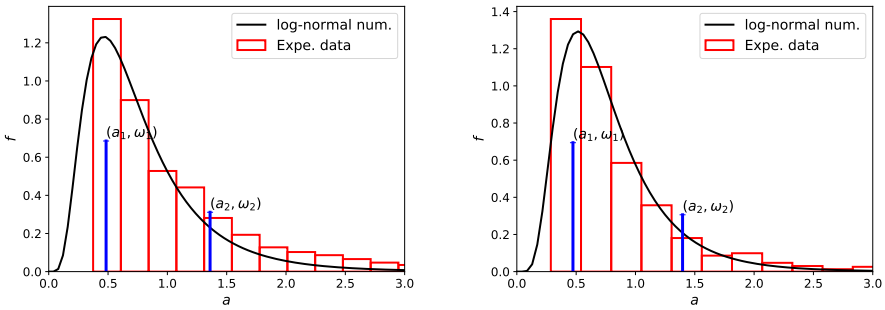

(c) T=1100 °C

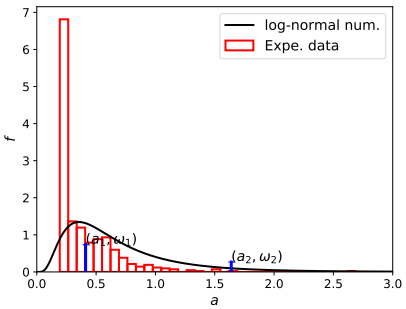

Figure 5: Normalized probability density function as a function of a determined from image analysis for the three temperatures at 120 min. Log-normal distribution and the amplitudes of ω_α are also reported for α equal 1 and 2.

perimental data. Numerical results are used to determine the bubble size distribution following a log-normal distribution. The three first moments of numerical solutions are needed to determine μ and σ of eq. (41). The zeroth moment is required to renormalize ω_α. The first and second moments allow to determine the mean and the standard deviation of the bubble size distribution. Figure 5 depicts the probability density function under histogram form obtained from image analysis for the three temperatures after a residence time in the furnace of 120 min. The log-normal distributions obtained from the numerical values of the first three moments are also plotted in solid line. The amplitude and position of each class are also provided. The comparison between experimental and numerical distributions is very good for the two first temperatures. For T=1100 °C, an over-representation in the smallest radius is observed. This large source of tiny bubbles is the result of the observation of Figure 1(f). This source of tiny bubbles could be an artificial bubble creation due to the post-morten treatment. It is particularly observed at this temperature and time because the total of bubbles are the smallest. Nevertheless, the decrease of the distribution as a function of the bubble radius is very well reproduced with the numerical results.

After two hours, the bubble size distribution does not change significantly. It is noteworthy to see that the numerical method allows to reproduce the probability density function. These results underline that the numerical method developed in this work is useful to describe the dynamics of bubble undergoing coalescence.

4.2. Fining process during the glass melting

Fining process is the limiting step in glass melting. As already pinpointed in section 1, the bubble removal in industrial plant is strongly enabled by the addition of "fining agents". Hujová and Vernerová [57, 58] did a review of this mechanism in which the various fining agents are presented. Since the bubble removal is mainly driven by the bubble rising, the addition of chemical species disolving gas when the temperature increases leads to a bubble growth. Moreover, the increase of temperature decreases the viscosity leading to an enhancement of the bubble rising velocity. The effect of sodium sulfate introduced in raw materials as Na_2SO_4 is studied in this subsection. According to Chopinet et al. [59], the following chemical reaction

$$Na_2SO_4 \longrightarrow Na_2O + SO_2(g) + \frac{1}{2}O_2(g) \tag{45}$$

is involved with "g" gas species. This last reaction is observed when the glass forming liquid is enough oxidized. For soda-lime-silicate glasses, the oxidation-reduction state is controlled by the quantity of the molecular oxygen, O_2, dissolved in the liquid. It depends on the redox state of the iron, the main transition metal found in industrial

glasses. The oxidation-reduction is then controlled by

$$\mathrm{Fe}^{3+} + \frac{1}{2}\mathrm{O}^{2-} \rightleftharpoons \mathrm{Fe}^{2+} + \frac{1}{4}\mathrm{O}_2(g). \tag{46}$$

Equation (45) can be also written in terms of ionic species as follows [59]

$$\mathrm{SO_4}^{2-} \longrightarrow \mathrm{SO}_2(g) + \frac{1}{2}\mathrm{O}_2(g) + \mathrm{O}^{2-}. \tag{47}$$

Knowing the redox state of the iron defined by

$$\mathcal{R}_{\mathrm{Fe}} = \frac{C^l_{\mathrm{Fe}^{2+}}}{C^l_{\mathrm{Fe}}}, \tag{48}$$

the oxygen concentration, in mol/m^3, dissolved in the glass forming liquid is then determined by

$$C^l_{\mathrm{O}_2} = \left[\frac{(1-\mathcal{R}_{\mathrm{Fe}})K_{\mathrm{Fe}}}{\mathcal{R}_{\mathrm{Fe}}}\right]^4, \tag{49}$$

in which K_{Fe} is the equilibrium constant of the chemical reaction (46). In (48), $C^l_{\mathrm{Fe}^{2+}}$ is the molar concentration of Fe^{2+} and C^l_{Fe} is the total molar concentration of iron equal to $C^l_{\mathrm{Fe}^{2+}} + C^l_{\mathrm{Fe}^{3+}}$, assumed constant all over the time.

From the reaction equilibrium of (47), the concentration of SO_2 dissolved in the liquid is given by

$$C^l_{\mathrm{SO}_2} = \frac{C^l_{\mathrm{S}} K_{\mathrm{S}}}{K_{\mathrm{S}} + \sqrt{C^l_{\mathrm{O}_2}}}, \tag{50}$$

in which K_{S} is the equilibrium constant of the reaction (47) and C^l_{S} is the total amount of sulfur introduced in the liquid.

Beside SO_2 and O_2 species, the nitrogen and carbon dioxide are generally dissolved in glass forming liquid. Since these two species come from the combustion atmosphere above the liquid bath and also from the carbon release of raw materials, the amount of N_2 and CO_2 dissolved in the glass forming liquid can be simply estimated by knowing the partial pressure in atmosphere above the glass bath [60]. This means that $C^l_{\mathrm{N}_2}$ and $C^l_{\mathrm{CO}_2}$ are given by

$$C^l_{\mathrm{N}_2} = \mathcal{L}_{\mathrm{N}_2} P_{\mathrm{N}_2}, \tag{51}$$

$$C^l_{\mathrm{CO}_2} = \mathcal{L}_{\mathrm{CO}_2} P_{\mathrm{CO}_2}. \tag{52}$$

One of the first contributions devoted to a quantitative analysis of the fining process has been done by Bastick [6]. He showed that the number of bubbles decreases expo-

T (°C)	$C^l_{SO_2}$ (mol/m^3)	$C^l_{O_2}$ (mol/m^3)	$C^l_{N_2}$ (mol/m^3)	$C^l_{CO_2}$ (mol/m^3)
1320	8.05	1.35×10^{-3}	1.24×10^{-2}	3.89×10^{-2}
1370	7.27	4.92×10^{-3}	1.41×10^{-2}	3.66×10^{-2}
1420	6.59	1.66×10^{-1}	1.58×10^{-2}	3.46×10^{-2}

Table 3: Molar concentration of gas species dissolved in a window glass for three temperatures.

nentially with time. The rate of bubble release increases with temperature but more quickly that expected from the effects of temperature on bubble size and viscosity. The numerical computations are applied to the equivalent situation studied by Bastick [6]. There are done for a window glass with 0.1 wt% of iron and a redox state equal to 0.23. The density is equal to 2350 kg/m^3 and the viscosity are given by

$$\eta(T) = 1.95 \cdot 10^{-3} \exp\left(\frac{9855.06}{T - 539.15}\right), \tag{53}$$

with T in Kelvin. The total amount of sulfur is set equal to 0.39 wt%. Partial pressure of N_2 and CO_2 are determined considering a combustion with air and natural gas. Equilibrium constants of reactions (46) and (47) and Henry coefficients are given in Appendix A. The initial molar concentrations for SO_2, O_2, N_2 and CO_2 determined with the above developments are reported in Table 3 for three temperatures considered in [6].

The numerical application considers a bubble population dispersed in a crucible obtained by the melting of raw materials or cullet [6]. The initial bubble density is set equal to 2×10^9 m^{-3}. Initially, the bubble size distribution is log-normal, see eq. (41), with $\sigma = 0.434$ and $\mu = -9.33$ given in meter. The initial volume fraction is equal to 1.35 % and the dimensionless parameter K_0 is equal to 2.2. Initially, bubbles are assumed to be composed of air, i.e. 21 % of O_2 and 79 % of N_2. The bubble population is described by taken N equal to 3.

Figure 6 depicts the zeroth order moment corresponding to the bubble density normalized by the initial value. The solid lines are obtained with the mass transfer. The dashed lines report the numerical results without mass transfer. The experimental results obtained by Bastick [6] have been provided in Figure 6 in solid circles. Colors are the same for all data. The absence of the mass transfer underestimates the bubble release. In dimensionless form, the behavior without mass transfer is completely similar for all temperatures. When the mass transfer is introduced, the bubble release enhances in large proportion. For both temperatures, the bubble density decreases quasi-exponentially. The bubble release is mainly driven by the rising of bubble and their escape from the free surface of the glass bath. If the increase of the bubble release would be due to the only viscosity, the behavior of μ_0 should be the same for both temperatures due to the

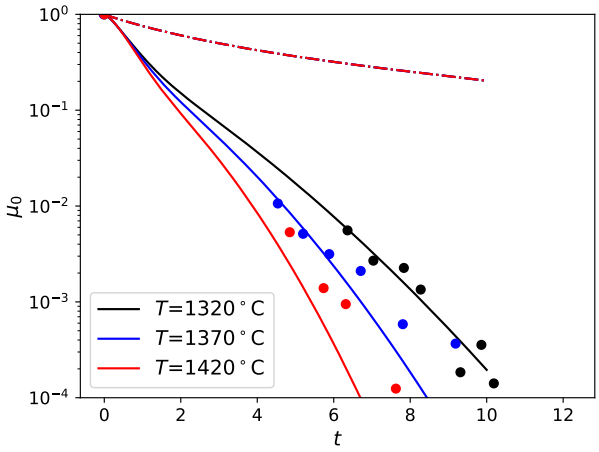

Figure 6: μ_0 as a function of dimensionless time for T=1320, 1370 and 1420 °C. Solid lines are obtained with mass transfer while dashed lines are determined without mass transfer. Experimental results obtained by Bastick [6] are plotted with solid circles.

normalization of time by the residence time of bubble with a radius a_0. Globally, the agreement with the experimental data of Bastick [6] is satisfying even if the numerical computation predicts a larger rate of decrease for T equal to 1370 and 1420 °C. Note that the experimental conditions of Bastick [6] have not clearly known. Few of data have been estimated to do the computations. The numerical computations reproduce well the fact that the bubble release rate increases faster that the temperature should be done. The addition of fining agent enhances the bubble release during the glass melting.

The Sauter mean radius determined as follows

$$r_{32} = \frac{\mu_3}{\mu_2} \tag{54}$$

is plotted as a function of time in Figure 7 for the three temperatures used in the numerical computations. It is noteworthy to see a non-monotonic behavior of r_{32} for both temperatures. At the early times, the growth rate is quasi similar for all temperatures. The maximum of bubble size differs with the temperature. The increase of the temperature leads to an increase of the Sauter mean radius. After a decrease of bubble size, an uniform growth rate is observed for a dimensionless time larger than 3. The growth rate is larger and larger when the temperature increases. For the smallest temperature, the Sauter mean radius is only 60 % larger than in the initial condition while for the largest temperature, the bubble size is multiplied by a factor of order 2.17 to the initial value.

Figure 8 depicts the size-conditioned molar fraction of the four gas species for the three values of α. Only results obtained for T=1320 °C are reported in Figure 8 since

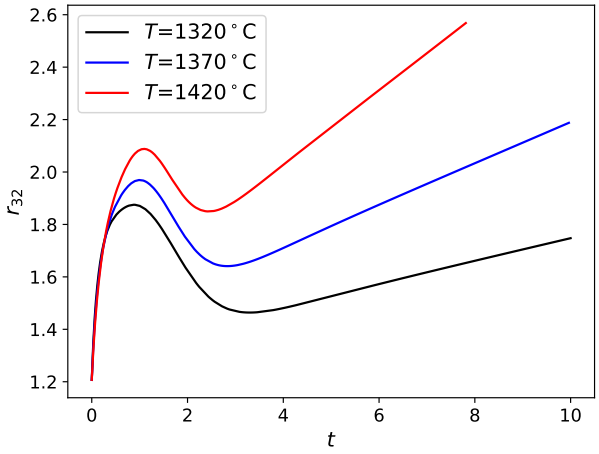

Figure 7: r_{32} as a function of dimensionless time for T=1320, 1370 and 1420 °C.

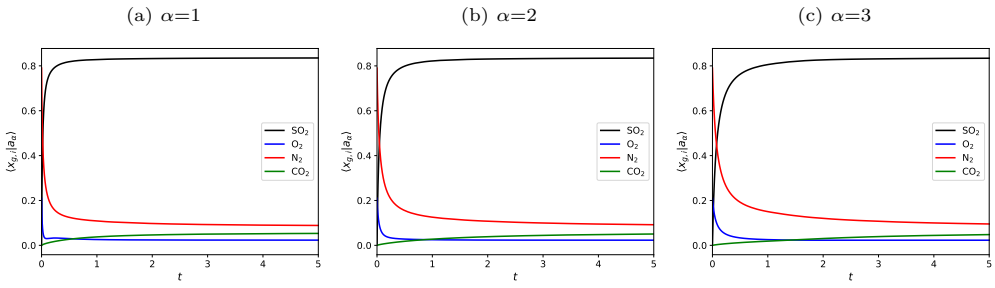

Figure 8: $\langle x_{g,i}|a_\alpha\rangle$ as function of dimensionless time at T=1320 °C for the four gas species and for the three classes.

the behavior of the molar fractions does not significantly change with the temperature. Initially composed by air, the bubble composition changes quickly. Nitrogen and oxygen are replaced by SO_2 gas species which is the most dissolved species. The mass transfer of SO_2 is very efficient due to a large value of the driver force at early stage. At long times, CO_2 becomes more significant than O_2. The final composition of bubbles is mainly given by SO_2, N_2 and CO_2. This result is in agreement with the simpler model developed in [26] for unique bubble initially composed by oxygen. This behavior on the bubble composition underlines that the dynamics of gas species differs for one species to another. The important factor in the mass transfer is the $\mathcal{H}_i \, \mathrm{Fo}_i$ corresponding to a gas permeability. For SO_2, O_2, N_2 and CO_2, these products are equal to 3.52, 3.76, 5.27×10^{-2} and 1.44×10^{-1} respectively. The change of composition is mainly due to the mass transfer of SO_2 and O_2 species. Even if the molar fraction of N_2 decreases in large proportion it is mainly due to the migration of SO_2.

Figure 9 presents the temporal behavior of the molar fraction of the four species dissolved in the glass forming liquid. Results obtained at the three temperatures are provided. Globally, the composition of dissolved gas species changes due to mass transfer from the liquid to bubble population. Apart from O_2 species, the dissolved gas species decrease with the time. For O_2 species, the non-monotonic behavior is due to the mass transfer of bubbles rich in oxygen at short times.

Theses results show the complex coupling between the two phases. As expected the bubble population can play important role in the chemistry of the liquid. The model developed in this work is able to quantify the mass transfer and the bubble release.

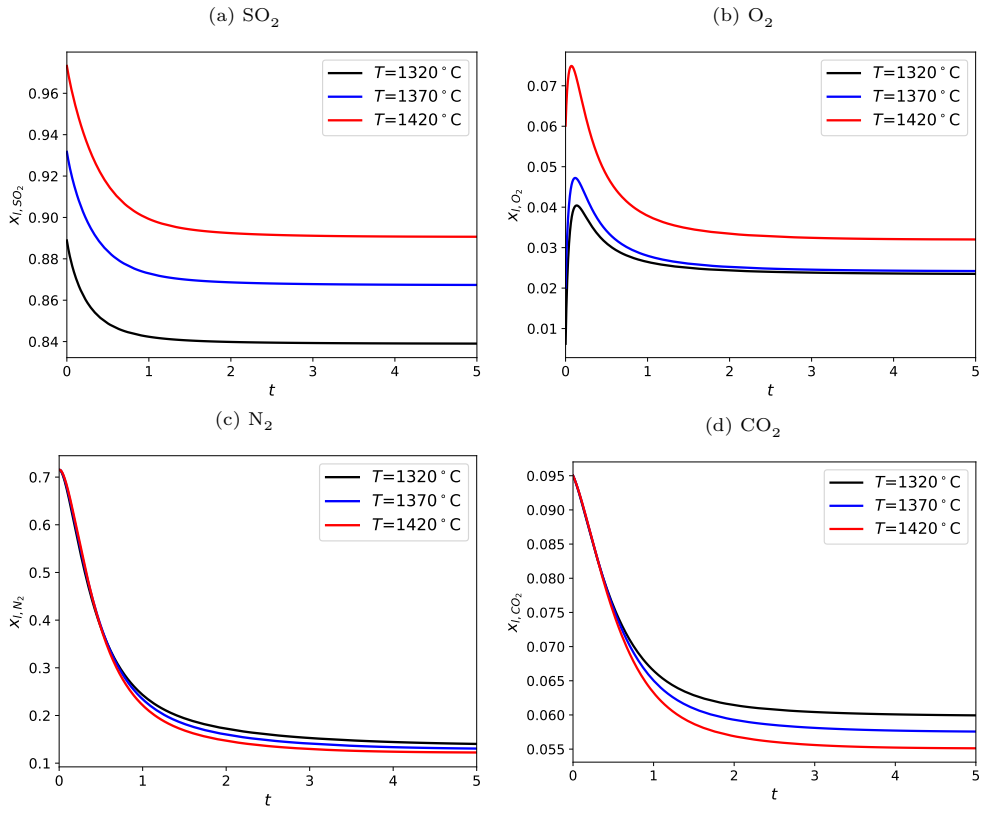

Figure 9: $x_{l,i}$ as function of dimensionless time four the three temperatures.

5. Synthesis and perspectives

To see the relevance of the bubble coalescence after the glass bead melting and the fining agents on the mass transfer, an original theoretical model based on a population balance equation is developed. Both mass transfer and coalescence are accounted for. To solve numerically the population balance equation, a direct quadrature method of moments (DQMOM) has been implemented. The numerical method is applied to experiments achieved by Pereira et al. [8] and by Bastick [6].

According to Pereira et al. [8], it was observed that the bubble density decreases strongly at short time. Using a coalescence kernel due to the relative rising of bubble, the numerical results well reproduce the experimental behavior. This underlines that the coalescence, as suggested by Cable [9], is the main mechanism of the bubble dynamics in a glass forming liquid. From the numerical results, it is possible to quantify this mechanism. The coalescence becomes significant when the bubble density is larger than $10^2\,\mathrm{cm}^{-3}$ or in other words, when the mean distance between inclusions gets shorter than 1 mm. Apart from the effect of coalescence, both experimental and numerical predictions allow to highlight that the bubble size distribution follows a log-normal law. This result already underlined by Boloré et al. [7] can be useful to follow the bubble dynamics in CFD software. The experimental data provided here can be used to determine the initial bubble size distribution.

The application of the numerical model in the case driven by the mass transfer is also efficient. The faster bubble release mentioned by Cable [10] is reproduced and explained. It is mainly due to the change of the glass chemistry with the temperature. The increase of gas release dissolved in the glass forming liquid is the most important phenomena explaining the bubble release. The important feature of the model developed in this work is the coupling with the liquid phase leading to the modification of the chemistry of the liquid.

The DQMOM method developed for this work allow to describe the mass transfer by writing balance equation of each molar fraction of relevant gas species dissolved in the liquid. As already presented in [24], it is possible to couple the bubble dynamics with the chemistry of the glass forming liquid. The future step is to develop this model in CFD software and applied it to furnace design. As it is well documented in the textbook of Marchisio and fox [14], DQMOM fails when it is applied to multidimensional cases. The conditional quadrature method of moments proposed by Yuan and Fox [61] could be a relevant choice to extend the work presented here. This work is a main issue since both two-phase flow and the coupling with the glass chemistry are poorly described in existing CFD tools to design glass furnaces.

The numerical software developed for this work is accessible following the link DQ-

MOM.

Appendix A. Numerical parameters used in the numerical computations

Appendix A.1. Henry coefficients

The solubility of a gas species i is written as a function of the temperature T as follows

$$\mathcal{L}_i = A_i^{\mathrm{sol}} \exp\left(\frac{B_i^{\mathrm{sol}}}{T}\right). \tag{A.1}$$

The constants A_i^{sol} and B_i^{sol} to determine solubilities of the four gas species have been taken from Beerkens [60] for the pressure in Pa and the molar concentration in mol/m^3. Table A.4 gathers values for the four gas species used in this work.

Species	O_2	SO_2	CO_2	N_2
A_i^{sol} (mol/m^3/Pa)	1.37×10^{-4}	6.44×10^{-7}	5.6×10^{-7}	1.1×10^{-5}
B_i^{sol} (K)	-6633	7860	3120	-6633

Table A.4: Values of A_i^{sol} and B_i^{sol} used to compute the Henry coefficient given by eq. (A.1) according to [60].

Appendix A.2. Diffusion coefficients

The diffusion coefficients of each species are determined as a function of temperature following the relation

$$\mathcal{D}_i = A_i^{\mathrm{diff}} \exp\left(-\frac{B_i^{\mathrm{diff}}}{T}\right), \tag{A.2}$$

for which A_i^{diff} and B_i^{diff} are provided in Table A.5.

Species	O_2	SO_2	CO_2	N_2
$A_{\mathrm{G}_i}^{\mathrm{diff}}$ (m^2/s)	4.2×10^{-3}	4.45×10^{-7}	1.92×10^{-5}	4.3×10^{-5}
$B_{\mathrm{G}_i}^{\mathrm{diff}}$ (K)	26 646	15 360	21 516	19 364

Table A.5: Values of A_i^{diff} and B_i^{diff} used to compute the coefficient coefficient given by eq. (A.2) according to [60].

Appendix A.3. Equilibrium constants

According to Kondepudi and Prigogine [62], the equilibrium constant is written as follows

$$K_r = \exp\left(-\frac{\Delta G_r}{RT}\right), \tag{A.3}$$

with the Gibbs energy given by

$$\Delta G_r = \Delta H_r - T\Delta S_r. \tag{A.4}$$

The numerical values of the enthalpy and entropy of cerium reaction, (42), iron reaction, (46), and sulfur reaction, (47), are reported in Table A.6. Equilibrium constants are written with the molar concentration of O_2. Consequently, the values of ΔH_r and ΔS_r provided in Table A.6 take into account the oxygen solubility.

Reaction	Ce	Fe	S
ΔH_r ($\mathrm{kJ\,mol^{-1}}$)	77.5	141	233
ΔS_r ($\mathrm{J\,mol^{-1}\,K^{-1}}$)	51.06	64.56	97.58

Table A.6: Enthalpy and entropy of Ce reaction, (42), from [55] and reactions (46) and (47) according to [60].

References

[1] H. M. Gonnermann and M. Manga. The Fluid Mechanics Inside a Volcano. *Annu. Rev. Fluid Mech.*, 39:321–356, 2007.

[2] G. Liger-Belair. The Physics and Chemistry behind the Bubbling Properties of Champagne and Sparkling Wines: A State-of-the-Art Review. *J. Agric. Food. Chem.*, 53(8):2788–2802, 2005.

[3] S. Seetharaman, A. McLean, R. Guthrie, and S. Sridhar, editors. *Treatise on process metallurgy*, volume 2. Elsevier, 2014.

[4] M. Ishii and T. Hibiki. *Thermo-fluid Dynamics of Two-phase Flow*. Springer, 2011.

[5] J. E. Shelby. *Introduction to glass science and technology*. The Royal Society of Chemistry, Cambridge, third edition, 2015.

[6] R. E. Bastick. Laboratory experiments on the refining of glass. In *Symposium sur l'affinage du verre*, pages 127–138, Paris, 1956.

[7] D. Boloré, M. Gibilaro, L. Massot, P. Chamelot, E. Cid, O. Masbernat, and F. Pigeonneau. X-ray imaging of a high temperature furnace applied to glass melting. *J. Am. Ceram. Soc.*, 103:979–992, 2020.

[8] L. Pereira, O. Podda, B. Fayard, A. Laplace, and F. Pigeonneau. Experimental study of bubble formation in a glass-forming liquid doped with cerium oxide. *J. Am. Ceram. Soc.*, 103:2453–2462, 2020.

[9] M. Cable. A study of refining. Part 2: Mechanisms of refining. *Glass Technol.*, 2:60–70, 1961.

[10] M. Cable. A century of developments in glassmelting research. *J. Amer. Ceram. Soc.*, 81:1083–1094, 1998.

[11] A. D. Randolph and M. A. Larson. Transient and steady state size distributions in continuous mixed suspension crystallizers. *AIChE J.*, 8(5):639–645, 1962.

[12] H. M. Hulburt and S. Katz. Some problems in particles technology. *Chem. Eng. Sci.*, 19:555–574, 1964.

[13] D. Ramkrishna. *Population balances. Theory and application to particulate systems in engineering*. Academic Press, San Diego, 2000.

[14] D. L. Marchisio and R. O. Fox. *Computational models for polydisperse particulate and multiphase systems*. Cambridge University Press, 2013.

[15] A. Ungan, W. H. Turner, and R. Viskanta. Effect of gas bubbles on three-dimensional circulation in a glass melting tank. *Glastechn. Ber.*, 56K:125–129, 1983.

[16] A. Ungan, R. U. Payli, and B. Balkanli. Numerical model of polydispersed silica grain dissolution in glass melting furnaces. *J. Am. Ceram. Soc.*, 77:1921–1927, 1994.

[17] T. Roi, O. Seidel, G. Nölle, and D. Höhne. Modeling of the bubble population in glass melt. *Glass Sci.Technol.*, 67:263–271, 1994.

[18] B. Balkanli and A. Ungan. Numerical simulation of bubble behaviour in glass melting tanks. Part 4. Bubble number density distribution. *Glass Technol.*, 37:164–168, 1996.

[19] A. Bensberg and C. Breitbach. Bubble continuum model. In *Advances in Fusion and Processing of Glass III*, Ohio, 2004.

[20] L. Pilon, A. G. Fedorov, D. Ramkrishna, and R. Viskanta. Bubble transport in three-dimensional laminar gravity-driven flow – mathematical formulation. *J. Non-Cryst. Solids*, 336:71–83, 2004.

[21] L. Pilon and R. Viskanta. Bubble transport in three-dimensional laminar gravity-driven flow – numerical results. *J. Non-Cryst. Solids*, 336:84–95, 2004.

[22] L. Pilon and R. Viskanta. Modified method of characteristics for solving population balance equations. *Int. J. Num. Meth. Fluids*, 42:1211–1236, 2003.

[23] K. Oda and M. Kaminoyama. Mathematical model of bubble number density in glass tank furnace. *J. Ceram. Soc. Jpn.*, 117(1366):736–741, 2009.

[24] F. Pigeonneau. Coupled modelling of redox reactions and glass melt fining processes. *Glass Technol.: Eur. J. Glass Sci. Technol. A*, 48(2):66–72, 2007.

[25] J. I. Ramos. Behavior of multicomponent gas bubbles in glass melts. *J. Am. Ceram. Soc.*, 69:149–154, 1986.

[26] F. Pigeonneau. Mechanism of mass transfer between a bubble initially composed of oxygen and molten glass. *Int. J. Heat Mass Transfer*, 54:1448–1455, 2011.

[27] S.-M. Yang and L. G. Leal. A note on memory-integral contributions to the force on an accelerating spherical drop at low reynolds number. *Phys. Fluids A*, 3(7):1822–1824, 1991.

[28] J. Magnaudet and D. Legendre. The viscous drag force on a spherical bubble with a time-dependent radius. *Phys. Fluids*, 10(3):550–554, 1998.

[29] J. Hadamard. Mouvement permanent lent d'une sphère liquide et visqueuse dans un liquide visqueux. *C. R. Acad. Sci. Paris*, 152:1735–1738, 1911.

[30] W. Rybczynski. Uber die fortschreitende bewegun einer flussingen kugel in einem zaben medium. *Bull. de l'Acad. des Sci. de Cracovie, série A*, 1:40–46, 1911.

[31] M. S. Plesset and A. Prosperetti. Bubble dynamics and cavitation. *Annu. Rev. Fluid Mech.*, 9(1):145–185, Jan 1977.

[32] V. G. Levich. *Physicochemical hydrodynamics*. Prentice Hall, Englewood Cliffs, N.J., 1962.

[33] R. Clift, J. R. Grace, and M. E. Weber. *Bubbles, Drops, and Particles*. Academic Press, New York, 1978.

[34] F. Pigeonneau, D. Martin, and O. Mario. Shrinkage of oxygen bubble rising in a molten glass. *Chem. Eng. Sci.*, 65:3158–3168, 2010.

[35] R. Sander. Compilation of Henry's law constants (version 4.0) for water as solvent. *Atmos. Chem. Phys.*, 15(8):4399–4981, 2015.

[36] R. Fan, D. L. Marchisio, and R. O. Fox. Application of the direct quadrature method of moments to polydisperse gas-solid fluidized beds. *Powder Technol.*, 139:7–20, 2004.

[37] Y. Liao and D. Lucas. A literature review on mechanisms and models for the coalescence process of fluid particles. *Chem. Eng. Sci.*, 65(10):2851–2864, 2010.

[38] X. Zhang and R. H. Davis. The rate of collisions due to brownian or gravitational motion of small drops. *J. Fluid Mech.*, 230:479–504, 1991.

[39] A. Z. Zinchenko. Calculation of the effectiveness of gravitational coagulation of drops with allowance for internal circulation. *Prikl. Matem. Mekhan.*, 46:72–82, 1982.

[40] A. Kovetz and B. Olund. The effect of coalescence and condensation on rain formation in a cloud of finite vertical extent. *J. Atmos. Sci.*, 26(5):1060–1065, 1969.

[41] F. Pigeonneau and F. Feuillebois. Collision and size evolution of drops in homogeneous isotropic turbulence. *J. Aerosol Sci.*, 29:S1279–S1280, 1998.

[42] F. Gelbard and J. H. Seinfeld. Numerical solution of the dynamic equation for particulate systems. *J. Comput. Phys.*, 28(3):357–375, 1978.

[43] D. Ramkrishna. Solution of population balance equations. *Chem. Eng. Sci.*, 26:1134–1136, 1971.

[44] D. Ramkrishna. The status of population balances. *Rev. Chem. Eng.*, 3(1):49–95, 1985.

[45] H. M. Hulburt and T. Akiyama. Liouville equations for agglomeration and dispersion processes. *I. & E. C. Fundamentals*, 8-2:319–324, 1969.

[46] D. L. Marchisio and R. O. Fox. Solution of population balance equations using the direct quadrature method of moments. *J. Aerosol Sci.*, 36:43–73, 2005.

[47] R. G. Gordon. Error bounds in equilibrium statistical mechanics. *J. Math. Phys.*, 9(5):655–663, 1968.

[48] J. C. Wheeler. Modified moments and gaussian quadratures. *Rocky Mt. J. Math.*, 4(2):287–296, 1974.

[49] D. L. Marchisio, R. D. Vigil, and R. O. Fox. Implementation of the quadrature method of moments in CFD codes for aggregation-breakage problems. *Chem. Eng. Sci.*, 58:3337–3351, 2003.

[50] L. Pereira, M. Vernerová, J. Kloužek, A. Laplace, and F. Pigeonneau. Experimental and numerical studies of an oxygen single-bubble shrinkage in a borosilicate melt doped with cerium oxide. *J. Am. Ceram. Soc.*, 103:6736–6745, 2020.

[51] H. Scholze. *Glass. Nature, Structures and Properties.* Springer-Verlag, Berlin, 1990.

[52] A. K. Varshneya and J. C. Mauro. *Fundamentals of Inorganic Glasses.* Elsevier, third edition, 2019.

[53] A. Baddeley and E. B. Vedel Jensen. *Stereology for statisticians.* Chapman and Hall/CRC, 2005.

[54] N. Reboul, E. Vincens, and B. Cambou. A statistical analysis of void size distribution in a simulated narrowly graded packing of spheres. *Granular Matter*, 10(6):457–468, 2008.

[55] O. Pinet, J. Phalippou, and C. Di Nardo. Modeling the redox equilibrium of the Ce^{4+}/Ce^{3+} couple in silicate glass by voltammetry. *J. Non-Cryst. Solids*, 352(50-51):5382–5390, 2006.

[56] M. Ungarish. *Hydrodynamics of suspensions.* Springer-Verlag, Berlin, 1993.

[57] M. Hujová and M. Vernerová. Influence of fining agents in glass melting: A review, part 1. *Ceramics-Silikáty*, 61(2):119–126, 2017.

[58] M. Hujová and M. Vernerová. Influence of fining agents in glass melting: A review, part 2. *Ceramics-Silikáty*, 61(3):202–208, 2017.

[59] M.-H. Chopinet, D. Lizarazu, and C. Rocanière. L'importance des phénomènes d'oxydo-réduction dans le verre. *C. R. Chimie*, 5(12):939–949, 2002.

[60] R. G. C. Beerkens. Analysis of advanced and fast fining processes for glass melts. In *Advances in Fusion and Processing of Glass III*, pages 3–24. American Ceramic Society, New York, 2004.

[61] C. Yuan and R. O. Fox. Conditional quadrature method of moments for kinetic equations. *J. Comput. Phys.*, 230(22):8216–8246, 2011.

[62] D. Kondepudi and I. Prigogine. *Modern Thermodynamics: From Heat Engines to Dissipative Structures.* John Wiley & Sons, New York, 2nd edition, 2015.